



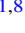




On the Connection between Rieger-type and Magneto-Rossby Waves Driving the Frequency of the Large Solar Eruptions during Solar Cycles 19–25

Marianna B. Korsós^{1,2,3,4} , Mausumi Dikpati⁵ , Robertus Erdélyi^{2,4,6} , Jiajia Liu⁷ , and Francesca Zuccarello^{1,8} ¹Dipartimento di Fisica e Astronomia “Ettore Majorana,” Università di Catania, Via S. Sofia 78, I-95123 Catania, Italy; kombabi@gmail.com²Department of Astronomy, Eötvös Loránd University, Pázmány Péter sétány 1/A, H-1112 Budapest, Hungary³Department of Physics, Aberystwyth University, Ceredigion, Cymru SY23 3BZ, UK⁴Hungarian Solar Physics Foundation, Petőfi tér 3, H-5700 Gyula, Hungary⁵High Altitude Observatory, NCAR, 3080 Center Green Drive, Boulder, CO 80301, USA⁶Solar Physics & Space Plasma Research Center (SP2RC), School of Mathematics and Statistics University of Sheffield, Hounsfield Road, Sheffield S3 7RH, UK⁷School of Earth and Space Sciences, University of Science and Technology of China, 96 JinZhai Road, Hefei 230026, People’s Republic of China⁸INAF—Catania Astrophysical Observatory, Via S. Sofia 78, I-95123 Catania, Italy

Received 2022 October 29; revised 2023 January 14; accepted 2023 January 24; published 2023 February 23

Abstract

Global solar activity variation mainly occurs over about an 11 yr cycle. However, both longer and shorter periodicities than the solar cycle are also present in many different solar activity indices. The longer timescales may be up to hundreds of years, while the shorter timescales for global solar variability could be within 0.5–2 yr, which include, e.g., from the Rieger-type periods (150–160 days) to quasi-biennial oscillations of 2 yr. The most likely origin of this short-timescale quasi-periodicity is attributed to magnetic Rossby waves, which have periods of 0.8–2.4 yr. In this work, we present findings of a unique evolution of identified shorter periodicities, like the Rieger-type, arising from magnetic Rossby waves, throughout Solar Cycles 19–25. We report further observational evidence of the strong relationship between the Rieger-type periodicity, magneto-Rossby waves, and major solar flare activity. Moreover, this study also reveals that the global solar magnetic field has a continuous periodic longitudinal conveyor belt motion along the solar equator, together with an up-and-down movement in the latitudinal directions. We found that when these longitudinal and latitudinal movements have Rieger-type periodicity and magneto-Rossby waves during the same period of a solar cycle, major flare activity is present.

Unified Astronomy Thesaurus concepts: [Active solar chromosphere \(1980\)](#)

1. Introduction

Rossby waves, which manifest as large meandering patterns, are planetary waves or a class of inertial waves, occurring in a rotating fluid shell owing to variation in the Coriolis force and pressure gradient with latitude. These waves were first identified by Rossby (1939). In the Sun, the Rossby waves (Gilman 1969a, 1969b) were found to be generated at/near the base of the convection zone, which provides a favorable environment for their generation and propagation. Recently, various observations have revealed evidence of solar Rossby waves (see, e.g., Zaqrashvili et al. 2015; McIntosh et al. 2017; Löptien et al. 2018). Motivated by these observations, elaborated theoretical and numerical studies are performed to understand and model solar Rossby waves, specifically their properties and interactions with the Sun’s zonal flow and magnetic fields (see Dikpati et al. 2018a; Zaqrashvili et al. 2021, for an extensive review). Therefore, the view is becoming more widely accepted that the magnetic Rossby waves could influence solar magnetic field activity on several timescales.

In the past two decades, various groups of researchers have embarked on establishing the theoretical foundations of the basic physical aspects of the magnetic Rossby waves. Zaqrashvili et al. (2007, 2009) studied the frequencies and propagation properties of this type of wave in the approximation of shallow water magnetohydrodynamics (MHD). They found that the magnetic

Rossby waves have two separate types of families. The first one is the fast magnetic Rossby mode, which is a hydrodynamic Rossby wave slightly modified by the magnetic field. The second one comprises the slow magnetic Rossby waves with significantly smaller frequencies. In a follow-up study, Zaqrashvili (2018) also suggested that the periodicities of all modes of the equatorial magnetic shallow water waves can be observed in various solar activities because the waves are equatorially trapped. The existence of equatorially trapped Rossby waves was confirmed by Liang et al. (2019) throughout the interval of Solar Cycles 23–24 (SC23–SC24).

Gilman & Dikpati (2014) and Gilman (2015) found that the shallow water and baroclinic instabilities are present at almost all the latitudes in the tachocline zone. They also revealed that these waves are absent at the poles. Further, a number of substantial works were carried out to develop the nonlinear theory of magneto-Rossby waves (e.g., Lou 1987; Raphaldini & Raupp 2015; Klimachkov & Petrosyan 2017; Raphaldini et al. 2019; Fedotova et al. 2021, and references therein).

An interesting angle, in the context of the present paper, is found in the works that have made short-to-medium-term connections between magneto-Rossby waves and the observed features of the global solar magnetic activity (e.g., Zaqrashvili et al. 2011; Dikpati et al. 2018b; Bilenko 2020; Teruya et al. 2022). One of the first observational detections of solar magneto-Rossby waves was by Zaqrashvili et al. (2015). They identified the periods of magnetic Rossby waves in the long-term evolution of sunspot numbers and also in the concentrations of cosmogenic radionuclides (¹⁰Be and ¹⁴C). Next, Gurgenshili et al. (2016) showed that the Rieger-type (Rieger et al. 1984) periodicity (~150–160 days) has a strong



Original content from this work may be used under the terms of the [Creative Commons Attribution 4.0 licence](#). Any further distribution of this work must maintain attribution to the author(s) and the title of the work, journal citation and DOI.

dependence on the solar activity level, which also has a strong connection with the fast magneto-Rossby waves (Zaqarashvili & Gurgenchashvili 2018).

The presence of Rieger-type periods was also identified in many solar activity indicators, such as in solar X-ray flares (e.g., Olokutuyi et al. 2019), sunspot number or area (e.g., Lean 1990; Carbonell & Ballester 1992; Xiang et al. 2021), the 10.7 cm radio flux (F10.7; e.g., Lean & Brueckner 1989), and total solar irradiance (e.g., Pap et al. 1990). Meanwhile, the Rossby waves were detected in some parameters of flares, coronal mass ejections, and prominences (Lou 2000; Lou et al. 2003; Bilenko 2014). The manifestation of Rossby waves has also been revealed in (i) the relationship of magnetic field and sunspot indices (Feng et al. 2017), (ii) the evolution of bright points (McIntosh et al. 2017), and (iii) 2800 MHz radio flux frequency (Mei et al. 2018).

Dikpati et al. (2017, 2018b) have shown that MHD Rossby waves can manifest themselves in nonlinear oscillations between their energy and that of the solar differential rotation in the tachocline or the bottom of the convection zone (called tachocline nonlinear oscillations). These oscillations typically have periods of 6–18 months, similar in duration to Rieger-type periodicities. They argued that these tachocline nonlinear oscillations could be generating the “seasons” of the Sun, the enhanced bursts of activity, followed by quieter periods, occurring also on timescales of 6–18 months. Recently, Dikpati & McIntosh (2020) compiled a list of observational evidence to link the occurrence of the strongest solar eruptions to Rossby waves in the short period range from 8 months to 2.4 yr.

Inspired by the above-listed results, we now investigate the spatial and temporal evolution of the line-of-sight (LOS) magnetic field based on synoptic maps of the observations of the Michelson Doppler Imager (MDI) on board the Solar and Heliospheric Observatory (SOHO) and the Helioseismic and Magnetic Imager (HMI) on board the Solar Dynamics Observatory (SDO) in the period of 1996–2022. We also study the McIntosh archive of synoptic maps between SC19 and SC23. Our study is aimed at searching for further evidence for a connection between Rieger-type and magneto-Rossby waves, as well as major solar flare activity periods during SC19–SC25.

The work is organized as follows: Section 2 describes the analyzed synoptic map data series from 1954 to 2022. Section 3 introduces and describes the applied tool for the analyses of the evolution of the synoptic maps’ data series. Section 4 discusses our findings for SC19–SC25. Key results and conclusions are given in Section 6.

2. Data

In order to reach our goal, we analyzed the evolution of synoptic maps. A synoptic map is a representation of the full solar surface using different observations from Earth’s viewing direction. In this work, we analyzed two types of synoptic maps: (i) magnetic synoptic maps (Section 2.1), and (ii) synoptic maps of solar features (Section 2.3).

2.1. SOHO and SDO Magnetic Synoptic Maps

First, we employed the SOHO/MDI and SDO/HMI Carrington rotation (CR) synoptic maps⁹ for our analyses. SOHO/MDI observed the full solar disk in Ni λ 6768 absorption lines, while SDO/HMI takes measurements in the

Fe I absorption line at 6173 Å. The SOHO/MDI magnetic synoptic maps are generated from 20 definitive level 1.8 observations. The SDO/HMI synoptic maps are constructed from 720 s cadence LOS magnetograms collected over a 27-day solar rotation, with near-central-meridian data from 20 magnetograms.

Very often, \sim 450 G is considered to be the separation boundary between weak and strong magnetic fields because of the Zeeman splitting (Landi Degl’Innocenti & Landi Degl’Innocenti 1977). Namely, below \sim 450 G the thermal broadening is more dominant than the Zeeman broadening. Accordingly, we analyzed the stronger component of magnetic fields of SOHO/MDI magnetic synoptic maps from CR 1908 to CR 2096. In the case of SDO/HMI strong magnetic field data, we incorporated the synoptic maps between CR 2097 and CR 2249. To investigate the evolution of the strong magnetic fields in the synoptic maps, we also adopted the consideration of the magnetic field strength above 450 G.

2.2. McIntosh Archive Synoptic Map

The recently released digitalized McIntosh archive¹⁰ consists of a set of hand-drawn synoptic maps by Patrick McIntosh from 1954 to 2009. These detailed maps include polarity inversion lines, filaments, sunspots, plages, and later even coronal holes over a 45 yr period from 1964 to 2009. This archive was also extended backward until 1954 with Kodaikanal synoptic maps (Makarov & Sivaraman 1986). This data set represents a unique record of the large-scale organization and variation of the Sun’s magnetic field over CR 1355–CR 2086.

2.3. Flare Catalogs

To identify the strong flare activity period(s) of each SC, we used two types of catalogs both from the space era and from times preceding this epoch:

1. The Geostationary Operational Environmental Satellite (GOES)¹¹ catalog covers an era from 1975 to 2022. In this catalog, the A/B/C/M and X flare classes are defined based on the near-Earth measurements of the maximum X-ray flux at wavelengths from 0.1 to 0.8 nm. M- and X-class flares are the strongest ones, also adopted for consideration here out of the five intensity flare classes. Therefore, in the presented work, only M- and X-class flares were taken into account for analyzing the strong flare activity period of each SC.
2. Before the space age, flares were observed using H α filters. Since the 1930s, H α flare classification has been based on the visible red spectral line of wavelength 656.28 nm (emitted by H atoms) and has ranked flares according to their appearance area in square degrees of heliocentric latitude (Benz 2008). The observed flares are classified as “S” for a small flare and by adding the number 1, 2, 3, and 4 for flares of different sizes. The numbers 3 and 4 mean that the visible area of the flare is larger than 12.5 deg². For our study, from 1954 to 1974, we considered only flares that have large visible areas

¹⁰ <https://www2.hao.ucar.edu/mcintosh-archive/four-cycles-solar-synoptic-maps>

¹¹ <https://www.ngdc.noaa.gov/stp/space-weather/solar-data/solar-features/solar-flares/x-rays/flare>

⁹ <http://jsoc.stanford.edu/jsocwiki/SynopticMaps>

Table 1
H α and X-ray Flare Classification Schemes, based on Bhatnagar & Livingston (2005)

| H α Scheme | | Soft X-Ray Scheme | |
|-------------------|---------------------------------|-------------------|---|
| Class | Area (10^{-6} Solar Disk) | Class | Peak flux ($1-8 \text{ \AA w m}^{-2}$) |
| S | 200 | A | $10^{-8}-10^{-7}$ |
| 1 | 200–500 | B | $10^{-7}-10^{-6}$ |
| 2 | 500–1200 | C | $10^{-6}-10^{-5}$ |
| 3 | 1200–2400 | M | $10^{-5}-10^{-4}$ |
| 4 | 2400– | X | $10^{-4}-$ |

(classes 3 and 4), based on the USAF Solar Observing Optical Network (SOON)¹² catalog.

The above two classification schemes could be matched with each other in general, as suggested in Table 1, based on Bhatnagar & Livingston (2005).

3. Data Preparation

First, let us construct an animation from the image series of strong magnetic field values ($>|450|$ G) of the SOHO/MDI and SDO/HMI CR synoptic maps.¹³ We also prepared animation from McIntosh archive synoptic maps, but without any limitations.¹⁴ By inspection of the two animations, we noticed a continuous periodic conveyor belt motion in the longitudinal direction (Carrington longitude, L) accompanied by an up-and-down movement in the latitudinal direction (Carrington latitude, B). There is also notable even visually the clockwise and counterclockwise rotational direction of the conveyor belt alternating with each other.

To study the above-noticed periodical longitudinal and latitudinal motions of the global magnetic field, we employed the Gunnar–Farnebäck dense optical flow technique (Farnebäck 2003) on the two synoptic map series between SC19 and SC25. This applied dense optical flow method takes into account all the points and detects the pixel intensity changes between two consecutive images. We computed the magnitude and direction (longitudinal and latitudinal) of the optical flow from the flow vectors. The results are recorded in an image with highlighted pixels.

Panels (a)–(b) of Figure 1 are the synoptic maps of CR 2156 and CR 2157, which were treated as images in Hue Saturation Value (HSV) scale. The strength of the HSV scale is set to 0–255. In Figures 1(a)–(b), the blue(ish) color represents the negative magnetic field values (< -450 G), while red(dish) is for the positive ones (>450 G).

To visualize the magnitude of the intensity changes in the longitudinal and latitudinal directions, we also used the HSV format. Panels (c)–(d) of Figure 1 are the visualization of the longitudinal and latitudinal changes, respectively, of the global magnetic field map between CR 2156 and CR 2157.

All the measured longitudinal (latitudinal) intensity changes on the HSV scale between two consecutive CRs were summed

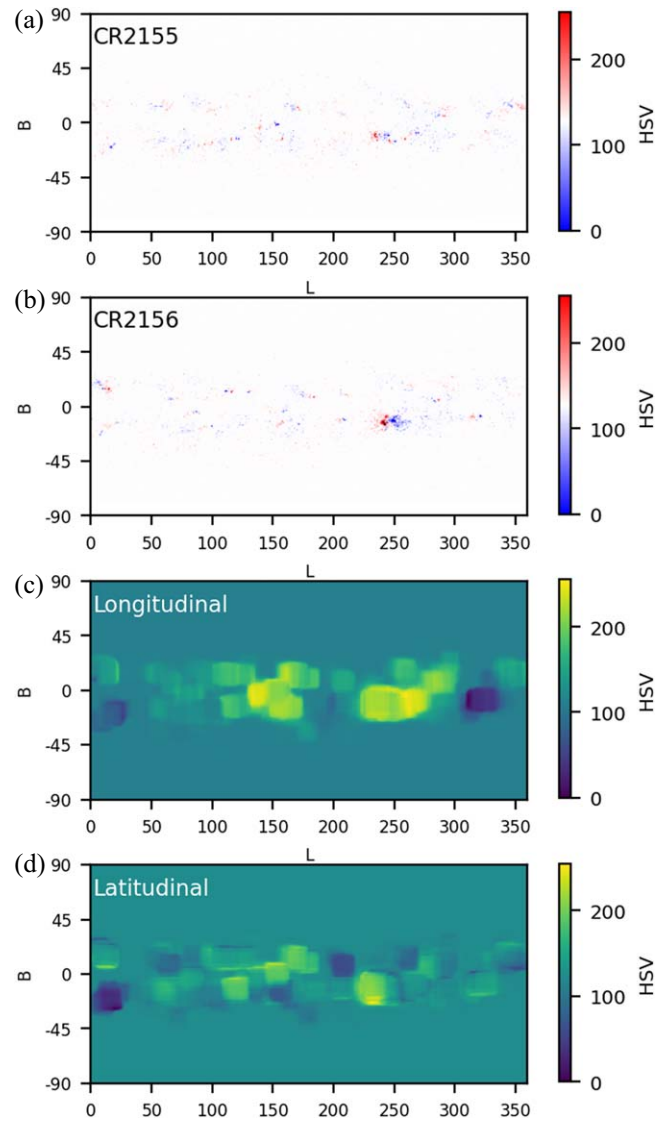


Figure 1. Panels (a)–(b) display the magnetic synoptic maps of CR 2156 and CR 2157. These two CR maps are treated as images on the 255 HSV scale. In these images, blue(ish) (0–127) represents the < -450 G magnetic values, while red(dish) (i.e., 128–255) is for the positive ones (>450 G). Panels (c)–(d) are the visualization of the (c) longitudinal and (d) latitudinal intensity changes of the global magnetic field map between CR 2156 and CR 2157. The magnitudes of the longitudinal and latitudinal intensity changes are also represented on the HSV scale, i.e., from 0 to 255.

as a next step. Therefore, we were able to obtain time series of the summed longitudinal intensity changes, as well as one for the corresponding latitudinal components.

Finally, to study the connection between the noted periodic movement of the longitudinal/latitudinal components and the major flare activity in each SC, we summed up the total number of M- and X-class (H α classes 3 and 4) flares of each month (MFN_{M+X}), like in the case of SC22 in Figure 2 (black curve). Next, we calculated the monthly average of MFN_{M+X} , which is represented with the blue line in Figure 2. After that, a major flare activity period of each investigated SC is considered when the MFN_{M+X} is larger than the monthly average. This period of SC22 is indicated by horizontal red lines in Figures 2–5. The beginning of the horizontal red line corresponds to the first time in which the FN_{M+X} exceeds the mean at the first moment of the corresponding SC, like in the case of SC22 in Figure 2. The

¹² <https://www.ngdc.noaa.gov/stp/space-weather/solar-data/solar-features/solar-flares/h-alpha/>

¹³ <https://drive.google.com/file/d/1zGYPCITGOcguo0Z8OHfUsDmlW23ZIQ3j/view?usp=sharing>

¹⁴ https://drive.google.com/file/d/1B_wE8K_1rVjNQuHSKggfvX3FaukaOP_/view?usp=sharing

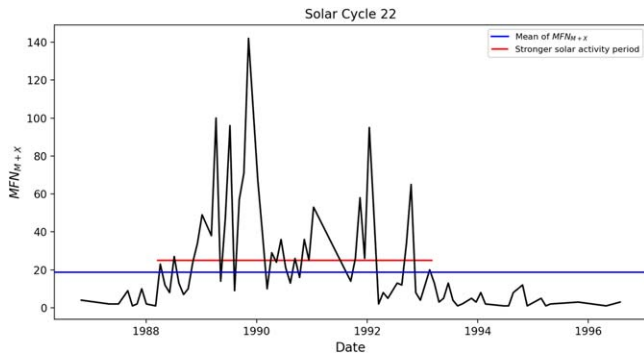


Figure 2. Total number of M- and X-class flares in each month (MFN_{M+X}) during SC22. The blue line is the mean of the MFN_{M+X} , which is considered as a threshold level to identify the large flare activity period of SC22.

end of the horizontal red line is when the MFN_{M+X} drops below the mean permanently, like in Figure 2.

4. Data Analysis

The time series of summed intensity changes in the longitudinal and latitudinal directions of each SC were further normalized (-1 to 1) by their respective largest value in order to facilitate comparison on similar scales, as shown in the top panels of Figures 3–5. We used the wavelet analyses software¹⁵ developed by Torrence & Compo (1998) to generate the wavelet power spectrum (WPS) of the time series of longitudinal and latitudinal data series with (i) red-noise background, (ii) zero-padding, and (iii) default Morlet wavelet profile. The associated global wavelet power spectrum (GPS) is also calculated as the time-averaged WPS. To identify the significant periods, the confidence level was set at 2σ .

To study the relationship between the Rieger-type periodicity, magneto-Rossby waves, and major solar flare activity, we classify the identified significant periods into two groups with

1. periods shorter than 200 days; and
2. periods longer than 200 days.

This classification is based on the empirical observation that there may not be a sharp boundary between the magnitude of the Rieger-type and magneto-Rossby waves periods, but some gaps still seem to exist.

In general, one could say that the Rieger-type periods (185–195 days, 150–160 days; see Gurgenchvili et al. 2016) and the periods of 128/102/78/51 days (that could even be generated in a similar way to the Rieger periods, or they may be harmonics of them; see Dimitropoulou et al. 2008) are found to be less than 200 days. In spite of their similarities, we do not yet have enough physical information about these shorter periods to label them undoubtedly as Rieger-type. Meanwhile, the magneto-Rossby waves with reported periods (e.g., ~ 240 days up to 2.4 yr; Dikpati & McIntosh 2020) are above 200 days.

4.1. SOHO and SDO Data

We first focus on the analysis of the magnetic synoptic maps of SC23 and SC24. In Figures 3(a)–(d), the top panels show the evolution of the time series of summed intensity changes in the longitudinal (panels (a) and (c)) and latitudinal (panels (b) and (d)) directions. The corresponding WPS and GPS plots of the

longitudinal and latitudinal components can be seen in the second and fourth rows of Figures 3(a)–(d), respectively. The actually obtained periods by WPS and GPS are also summarized in Table 2.

Based on Figures 3(a)–(d) and Table 2, we found the following:

1. *SC24*: In Figures 3(a)–(b), the WPSs and GPSs reveal periods both 200 days shorter and 200 days longer in the evolution of the longitudinal and latitudinal components. In the evolution of the longitudinal component, we identified three periods that are shorter than 200 days (~ 64.8 , 112.8 , and 165.2 days) and two longer ones (~ 1.7 and 3.2 yr). Similar to the longitudinal component, we found three periods shorter than 200 days (~ 71.9 and 105.3 days) and two periods longer than 200 days (~ 0.9 and 1.7 yr). Interestingly, major flare activity is present (red vertical line in Figures 3(a)–(b)) when *both* the shorter and longer periods are there in the evolution of the longitudinal and latitudinal components during the same period of SC24.
2. *SC23*: Similar to SC24, the WPS and GPS reveal the two types of periods in the evolution of the two components in Figures 3(c)–(d). For the longitudinal component, we identified two periods shorter than 200 days (~ 95.5 and 148.9 days) and two longer ones (~ 0.8 and 1.8 yr). Meanwhile, there are one shorter (~ 85.5 days) and three longer periods (~ 0.6 , 1.2 , and 2.2 yr) in the time series of the latitudinal component. Similar to SC24, the major flare activity happened (red vertical line in Figures 3(c)–(d)) during that period of the SC when the longitudinal and latitudinal components show *concurrent* periods of oscillations, in the case of both shorter and longer than 200 days.

4.2. McIntosh Archive Data

We also analyzed the series of the McIntosh archive synoptic maps between SC19 and SC23, similar to Section 4.1. Note that these synoptic maps include solar features rather than magnetic field data. To identify the major flare activity of each investigated SC, we used the GOES flare catalog from 1975. For times earlier than 1975, we used the SOON flare catalog.

In Figures 4(a)–(i), the corresponding WPS and GPS are visualized. Analyses of the longitudinal and latitudinal components also revealed oscillations with periods both shorter and longer than 200 days in the time series of the synoptic maps of the McIntosh archive. The corresponding measured periods can be found in Table 3.

Similar to the findings of Section 4.1, the major flare activity happened (see the horizontal red lines in Figures 4(a)–(i)) when, for the cases of periods both shorter and longer than 200 days, the longitudinal and latitudinal components can be found during the *same duration of evolution* of each SC. The best counterexample is SC22, when the longitudinal component does not have these shorter/longer periods after 6 yr from the beginning of the SC22; meanwhile, the latitudinal component does show the two types of periods throughout that SC.

Actually, SC22 is a very notable one. This SC had the shortest rise (34 months) from minimum to maximum compared to other SCs, based on the SC reports¹⁶ of the Australian Space Weather Forecasting Centre. The maximum

¹⁵ <https://github.com/chris-torrence/wavelets>

¹⁶ <https://www.sws.bom.gov.au/Educational/2/3/2>

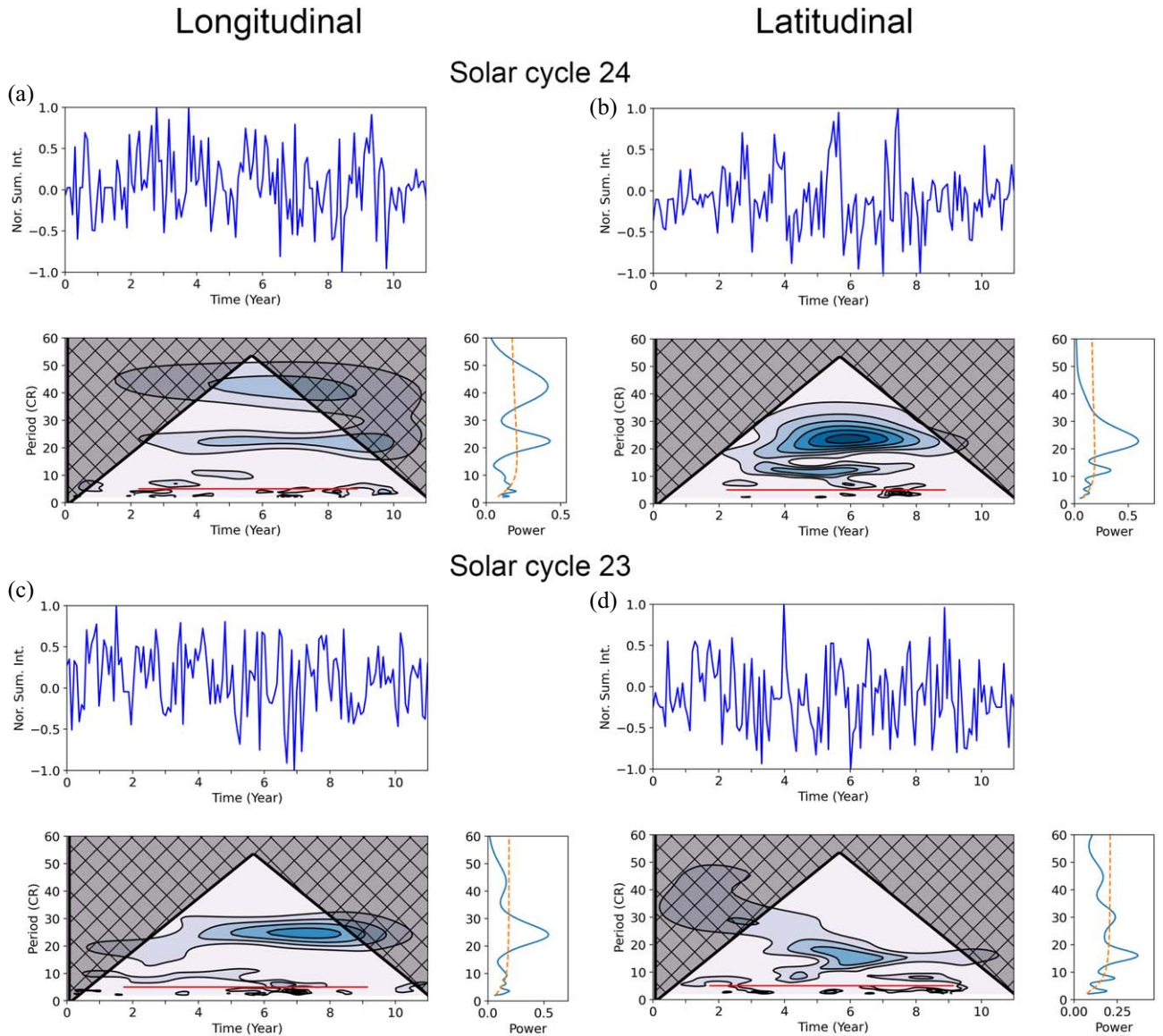


Figure 3. Panels (a)–(b) relate to SC23, while panels (c)–(d) refer to the analysis of SC24, based on the SOHO and SDO magnetic synoptic maps. The magnetic field is capped larger than $|450|$ G. The top panels show the evolution of the time series of summed intensity changes in the (a, c) longitudinal and (b, d) latitudinal directions of SC23 and SC24, respectively. The corresponding WPS and GPS analyses of the longitudinal and latitudinal components can be seen in the second and fourth rows, respectively. The periods are measured in CR. The red lines in the WPS plots mark the elapsed time between the appearance of the first X-class flare and the last X-class flare of the corresponding SC. In the WPS plots, the hatched black lines bound the cone of influence. The contour encloses regions that are greater than the 2σ confidence level for a red-noise process. The contour lines in the WPS plots indicate a rising significance ratio.

phase was a cradle to some extraordinary solar eruption activities. Prime among these was the 1989 March period, when a severe geomagnetic storm caused the collapse of Hydro-Québec’s electricity transmission system, an event widely addressed in the public domain given the implication and vulnerability of our infrastructures to space weather (Riley et al. 2018).

5. Notes on Beginning of Solar Activity

Solar flares originate mostly from solar active regions (ARs). The ARs in the solar surface are the areas where the small-scale magnetic flux aggregates and becomes especially strong across an extended area. Therefore, let us now also focus on the strong magnetic fields of SOHO/MDI and SDO/HMI magnetic synoptic maps. In particular, let us investigate at what point in time the first major flare activity

month occurred, in the context of the beginning of the formation of the periods (i.e., both shorter and longer than 200 days) discussed above.

Following on the identified shortest period that is longer than 200 days (i.e., ~ 0.7 – 1.2 yr) discussed in Section 4.1, let us now study each of the first 2.5 yr of the beginning of SC23, SC24, and SC25. The choice of length of 2.5 yr will also comply with the Nyquist frequency criteria.

In the case of SC25 and SC23, we identified the formation of periods of oscillations both less and greater than 100 days in the evolution of longitudinal and latitudinal components from the beginning of two SCs; see Figures 5(a)–(b) and (e)–(f). We note that the first major flare activity month appeared about 1.5 yr later when oscillation with period >100 days appeared, during the evolution of the longitudinal and latitudinal components.

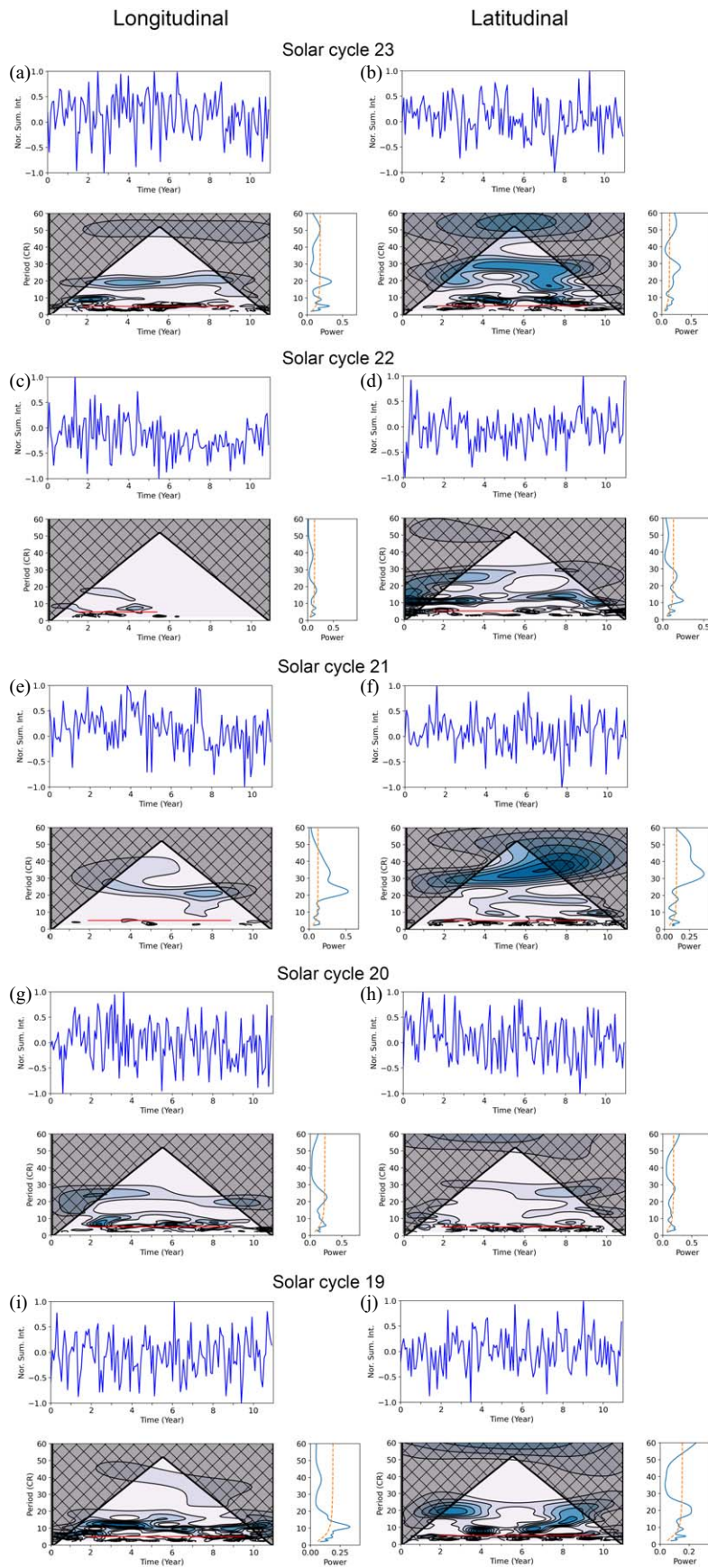


Figure 4. Similar to Figure 3, but derived from McIntosh archive data for the period SC19–SC23.

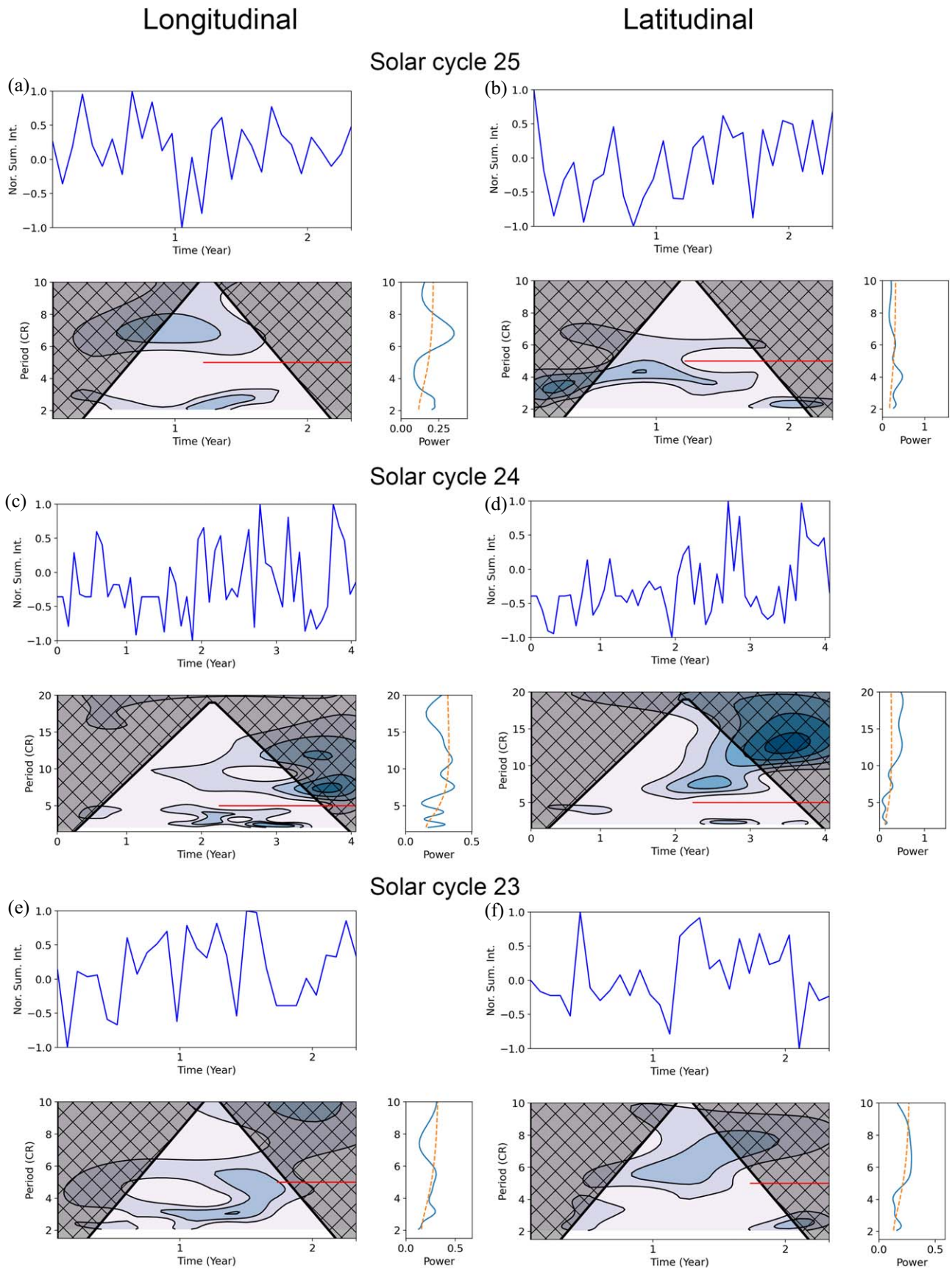


Figure 5. Similar to Figures 3 and 4, but here analyzing the beginning of SC23–SC25 employing SOHO and SDO magnetic synoptic maps.

Table 2

Actual Measured Periods in the Evolution of the Longitudinal and Latitudinal Directions by WPS and GPS in the Corresponding SC23 and SC24, Based on Figure 3

| SC | Longitudinal | | | Latitudinal | | |
|----|--------------|--------|-------|-------------|-------|-------|
| | CR | Days | Years | CR | Days | Years |
| 24 | 2.4 ± 7% | 64.8 | 0.2 | 2.6 ± 5% | 71.9 | 0.2 |
| | 4.1 ± 8% | 112.8 | 0.3 | 3.9 ± 7% | 105.3 | 0.3 |
| | | | | 12.1 ± 11% | 330.3 | 0.9 |
| | 22.6 ± 11% | 616.4 | 1.7 | 22.6 ± 14% | 616.4 | 1.7 |
| | 42.1 ± 16% | 1149.3 | 3.2 | | | |
| 23 | 3.5 ± 11% | 95.5 | 0.26 | 3.1 ± 9% | 85.5 | 0.2 |
| | 6.5 ± 8% | 148.9 | 0.4 | | | |
| | 10 ± 7% | 277.8 | 0.8 | 7.7 ± 9% | 210.5 | 0.6 |
| | 24.1 ± 12% | 664.1 | 1.8 | 16.0 ± 11% | 435.9 | 1.2 |
| | | | | 29.8 ± 11% | 813.3 | 2.2 |

Note. The first column is the SC number. The second through fourth columns include the measured periods of longitudinal movement in CR/days/years. The fifth through seventh columns include the measured periods of latitudinal movement in CR/days/years. The errors on the periods are estimated by jackknife estimation, based on Kirby & Swain (2013).

Table 3

Summary of the Found Periods in the Evolution of the Longitudinal and Latitudinal Directions, by WPS and GPS, in the Corresponding Solar Cycles from SC19 to SC23 Based on Figure 4

| SC | Longitudinal | | | Latitudinal | | |
|----|--------------|-------|-------|-------------|-------|-------|
| | CR | Days | Years | CR | Days | Years |
| 23 | 3.0 | 83.8 | 0.2 | 3.4 | 93.0 | 0.3 |
| | 5.3 | 145.9 | 0.4 | 6.5 | 179.6 | 0.5 |
| | 9.2 | 254.0 | 0.7 | 8.9 | 245.4 | 0.7 |
| | 19.7 | 544.5 | 1.5 | 19.0 | 525.9 | 1.4 |
| | | | | 27.7 | 756.2 | 2.1 |
| 22 | 3.2 | 89.8 | 0.2 | 2.5 | 70.5 | 0.2 |
| | | | | 5.1 | 140.9 | 0.4 |
| | 7.4 | 206.3 | 0.6 | 11.3 | 312.7 | 0.9 |
| | 17.7 | 490.7 | 1.3 | 25.9 | 718.4 | 2.0 |
| 21 | 2.9 | 80.9 | 0.2 | 2.4 | 65.7 | 0.2 |
| | 4.1 | 114.5 | 0.3 | 4.0 | 110.6 | 0.3 |
| | 9.2 | 254.0 | 0.7 | 9.5 | 263.0 | 0.7 |
| | 12.5 | 347.0 | 1.0 | 17.7 | 490.7 | 1.3 |
| | 22.6 | 625.4 | 1.7 | | | |
| | 33.0 | 900 | 2.4 | 33 | 900 | 2.4 |
| 20 | 2.2 | 60.5 | 0.2 | 3.5 | 94.9 | 0.3 |
| | 3.6 | 98.2 | 0.3 | 4.7 | 129.6 | 0.4 |
| | 6.0 | 165.2 | 0.5 | | | |
| | 22.6 | 616.4 | 1.7 | 27.8 | 758.9 | 2.1 |
| 19 | 2.7 | 75.5 | 0.2 | 2.8 | 78.2 | 0.2 |
| | 4.7 | 131.5 | 0.4 | 4.7 | 131.5 | 0.4 |
| | 6.9 | 192.5 | 0.5 | | | |
| | 10.9 | 302.1 | 0.8 | 8.9 | 245.4 | 0.7 |
| | | | | 19.7 | 544.5 | 1.5 |

In the case of SC24, we had to extend the investigated period from 2.5 to 4 yr because the periods of longitudinal and latitudinal components started to form about 1.5 yr later from the moment the SC had started; see Figures 5(c)–(d), which visually summarize the findings. Here we found that the first major flare activity month occurred about a year later after an

Table 4

Summary of the Identified Periods in the Evolution of the Longitudinal and Latitudinal Directions by WPS and GPS in the Corresponding Solar Cycles from SC23 to SC25 Based on Figure 5

| SC | Longitudinal | | | Latitudinal | | |
|----|--------------|-------|-------|-------------|-------|-------|
| | CR | Days | Years | CR | Days | Years |
| 25 | 2.6 | 71.9 | 0.2 | 2.3 | 62.79 | 0.17 |
| | | | | 4.0 | 109.0 | 0.3 |
| | 6.7 | 183.3 | 0.5 | 6.0 | 165.2 | 0.5 |
| 24 | 2.5 | 67.1 | 0.2 | 2.3 | 62.6 | 0.2 |
| | 4.1 | 112.8 | 0.3 | | | |
| | 7.7 | 210.5 | 0.6 | 7.2 | 196.4 | 0.5 |
| | 11.3 | 308.2 | 0.8 | 13.0 | 354.0 | 1.0 |
| 23 | 3.1 | 85.5 | 0.2 | 2.5 | 68.3 | 0.2 |
| | 5.5 | 148.9 | 0.4 | 6.5 | 177.0 | 0.5 |

oscillation with period greater than 100 days started to form during the *concurrent* evolution in both components.

In brief summary, based on Figure 5 and Table 4, we may conclude that the first major flare activity month of each SC appeared about 1–1.5 yr later with respect to when *concurrent* oscillations with periods >100 days started to develop, in both the longitudinal and latitudinal components.

6. Summary

Nowadays, it is becoming a more widely accepted hypothesis that the Rieger-type and magnetic Rossby waves have some important connections with the solar magnetic field activity on several timescales. Furthermore, it was also discovered that the Rieger-type periodicity (~150–160 days) has a strong connection with the fast magneto-Rossby waves (Zaqarashvili & Gurgenchashvili 2018). Similar to the Rieger-type periods, the magneto-Rossby waves have links to the occurrence of the strongest solar eruptions, especially their shorter periods, from, e.g., 240–270 days to 2.4 yr (Dikpati & McIntosh 2020).

Inspired by these abovementioned results and claims, here we investigated the evolution of the magnetic synoptic maps from 1996 to 2022 and synoptic maps of solar features from 1954 to 2009. The magnetic synoptic maps are based on LOS magnetic field measurements of SOHO/MDI and SDO/HMI observations. For the synoptic maps of solar features, we studied the McIntosh archive data between SC19 and SC23.

From the series of the synoptic maps of SC19–SC25, we identified a continuous periodic conveyor belt motion of the global magnetic field in the longitudinal direction, i.e., of the Carrington longitude (L), accompanied by an up-and-down movement in the latitudinal direction (Carrington latitude, B). To study this two-way periodic movement of the global magnetic field, we used a so-called Gunnar–Farnebäck dense optical flow technique (Farnebäck 2003) between each pair of consecutive images to measure the intensity changes in the longitudinal and latitudinal direction, respectively. Next, we determined the periodicities of intensity changes in the longitudinal and latitudinal directions. The obtained periods of each SC are summarized in Tables 2–3.

Let us here summarize the key points and the results found:

1. First, this study revealed that the global solar magnetic field has a continuous periodic conveyor belt motion

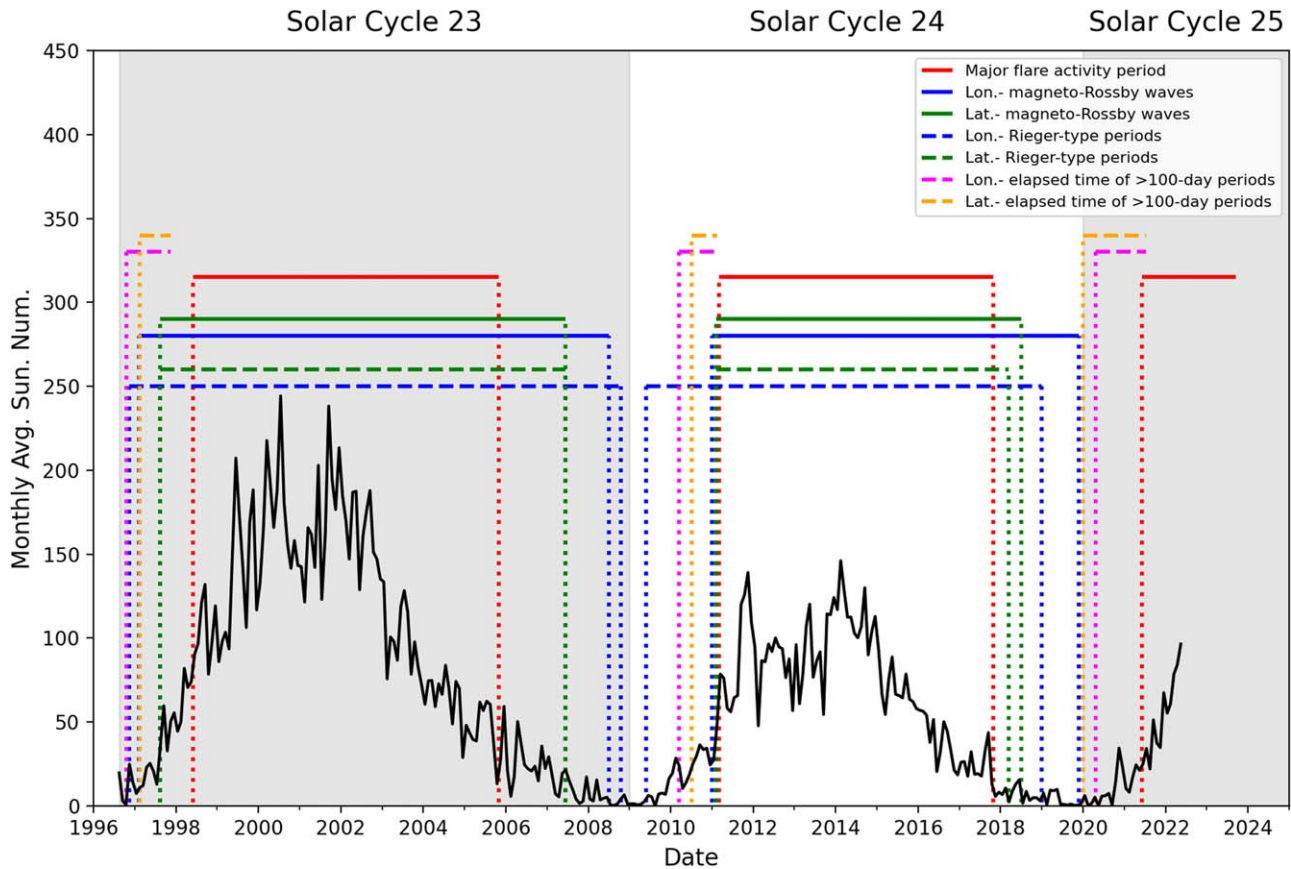


Figure 6. Visual summary of the main findings of the work. The black curve is the monthly mean total sunspot number from the beginning of SC23 until 2022 May. The red vertical line represents the major flare activity period of SC23, SC24, and SC25. The blue/green vertical line refers to the identified periods of the magneto-Rossby waves in the longitudinal/latitudinal movement of the global magnetic field in Figures 3(c)–(d), during SC23–SC24. The blue/green vertical dashed line refers to identified periods of Rieger-type in the longitudinal/latitudinal movement of the global magnetic field in Figures 3(c)–(d), during SC23–SC24. The short magenta/orange vertical dashed line refers to the elapsed time of the >100-day period in the longitudinal/latitudinal movement before the first X-class flare occurred in each SC, based on Figure 5.

along the solar equator (longitudinal direction), together with an up-and-down movement between the poles (latitudinal direction).

- There are oscillatory periods shorter than 200 days in both the longitudinal and latitudinal movements during each SC. These shorter periods are very similar to the Rieger-type periods (185–195 days, 150–160 days; see Gurgenchvili et al. 2016), and the periods of 128/102/78/51 days (which could even be generated in a similar way to the Rieger periods, or they may be harmonics of them; see Dimitropoulou et al. 2008) are found to be less than 200 days.
- We also identified oscillatory periods longer than 200 days, again in both the longitudinal and latitudinal periodic movements of each SC. These longer periods, however, are rather similar to those of the so-called magneto-Rossby waves.
- In Figure 6, one can see that, when the latitudinal and longitudinal movements have magneto-Rossby waves (blue/green line) and Rieger-type periods (blue/green dashed line) during the same epoch of each SC, the frequency of the large solar eruptions becomes significant (red line). This finding is in good agreement with the results of Dikpati & McIntosh (2020), who reported on the strong relationship between the occurrence of the strong solar eruptions and Rossby waves. In addition, this

feature can be seen in Figures 3–4, but the most supportive example is SC22. Another good example for supporting this finding may be seen during SC24.

- We also focused on the beginning of SC23–SC25 via studying the evolution of strong magnetic fields, derived from SOHO/MDI and SDO/HMI magnetic synoptic maps. Based on Figures 5–6, we found that the first major flare activity month of each SC appeared about 1–1.5 yr later once the periods of ~ 100 –200 days start to form, in both the longitudinal and latitudinal components.

The primary focus of our results shown above has been on periods of oscillations in various observed measures of solar activity. Some of these oscillation periods may be connected to the tachocline nonlinear oscillations simulated by Dikpati et al. (2017, 2018a). However, since all the data sets we have used are in the form of longitude–latitude synoptic maps, they can also be used to measure the longitudinal propagation speeds of persistent magnetic features. These speeds can then be compared to the expected speeds of HD and MHD Rossby waves likely to be present in the tachocline, as was done in Dikpati et al. (2018b) for coronal brightness patterns. This will be examined in a forthcoming paper.

We thank the anonymous referee, whose comments made this article easier to understand. M.K., F.Z., and R.E. acknowledge support from the European Union’s Horizon

2020 research and innovation program under grant agreement Nos. 739500 (PRE-EST project) and 824135 (SOLARNET project) and ISSI-BJ (“Step forward in solar flare and coronal mass ejection (CME) forecasting”). M.K. and F.Z. acknowledge support by the Università degli Studi di Catania (PIA.CE.RI. 2020–2022 Linea 2) and by the Italian MIUR-PRIN grant 2017APKP7T on “Circumterrestrial Environment: Impact of Sun-Earth Interaction.” This research was carried out in the framework of the CAESAR (Comprehensive spAce wEather Studies for the ASPIS prototype Realization) project, supported by the Italian Space Agency and the National Institute of Astrophysics through the ASI-INAF agreement no. 2020-35-HH.0 for the development of the ASPIS (ASI Space weather InfraStructure) prototype of scientific data center for Space Weather. M.B.K. is also grateful to the Science and Technology Facilities Council (STFC; UK, Aberystwyth University, grant No. ST/S000518/1), for the support received while conducting this research. R.E. is grateful to STFC (UK, grant No. ST/M000826/1). M.B.K. acknowledges support by UNKP-22-4-II-ELTE-186, ELTE Hungary. M.D. acknowledges support from the National Center for Atmospheric Research, which is a major facility sponsored by the National Science Foundation under cooperative agreement 1852977. M. D. also acknowledges partial support from NASA grants, such as NASA-LWS award 80NSSC20K0355 (awarded to NCAR) and NASA-HSR award 80NSSC21K1676 (awarded to NCAR). J.L. acknowledges support from the Informatization Plan of the Chinese Academy of Sciences (grant No. CAS-WX2021PY-0101), the National Key Technologies Research and Development Program of the Ministry of Science and Technology of China (2022YFF0711402), and the NSFC Distinguished Overseas Young Talents Program.

ORCID iDs

Marianna B. Korsós  <https://orcid.org/0000-0002-0049-4798>

Mausumi Dikpati  <https://orcid.org/0000-0002-2227-0488>

Robertus Erdélyi  <https://orcid.org/0000-0003-3439-4127>

Jiajia Liu  <https://orcid.org/0000-0003-2569-1840>

Francesca Zuccarello  <https://orcid.org/0000-0003-1853-2550>

References

- Benz, A. O. 2008, *LRSP*, **5**, 1
 Bhatnagar, A., & Livingston, W. 2005, *Fundamentals of Solar Astronomy*, Vol. 6 (Singapore: World Scientific)

- Bilenko, I. A. 2014, *SoPh*, **289**, 4209
 Bilenko, I. A. 2020, *ApJL*, **897**, L24
 Carbonell, M., & Ballester, J. L. 1992, *A&A*, **255**, 350
 Dikpati, M., Belucz, B., Gilman, P. A., & McIntosh, S. W. 2018a, *ApJ*, **862**, 159
 Dikpati, M., Cally, P. S., McIntosh, S. W., & Heifetz, E. 2017, *NatSR*, **7**, 14750
 Dikpati, M., & McIntosh, S. W. 2020, *SpWea*, **18**, e02109
 Dikpati, M., McIntosh, S. W., Bothun, G., et al. 2018b, *ApJ*, **853**, 144
 Dimitropoulou, M., Moussas, X., & Strintzi, D. 2008, *MNRAS*, **386**, 2278
 Farneback, G. 2003, *Two-Frame Motion Estimation Based on Polynomial Expansion*, 2749 (Berlin: Springer), 363
 Fedotova, M., Klimachkov, D., & Petrosyan, A. 2021, *Univ*, **7**, 87
 Feng, S., Yu, L., Wang, F., Deng, H., & Yang, Y. 2017, *ApJ*, **845**, 11
 Gilman, P., & Dikpati, M. 2014, *ApJ*, **787**, 60
 Gilman, P. A. 1969a, *SoPh*, **8**, 316
 Gilman, P. A. 1969b, *SoPh*, **9**, 3
 Gilman, P. A. 2015, *ApJ*, **801**, 22
 Gurgenchvili, E., Zaqarashvili, T. V., Kukhianidze, V., et al. 2016, *ApJ*, **826**, 55
 Kirby, J. F., & Swain, C. J. 2013, *GeoJI*, **194**, 78
 Klimachkov, D. A., & Petrosyan, A. S. 2017, *JETP*, **125**, 597
 Landi Degl’Innocenti, E., & Landi Degl’Innocenti, M. 1977, *A&A*, **56**, 111
 Lean, J. 1990, *ApJ*, **363**, 718
 Lean, J. L., & Brueckner, G. E. 1989, *ApJ*, **337**, 568
 Liang, Z. C., Gizon, L., Birch, A. C., & Duvall, T. L. 2019, *A&A*, **626**, A3
 Löptien, B., Gizon, L., Birch, A. C., et al. 2018, *NatAs*, **2**, 568
 Lou, Y. Q. 1987, *ApJ*, **322**, 862
 Lou, Y. Q. 2000, *ApJ*, **540**, 1102
 Lou, Y. Q., Wang, Y. M., Fan, Z., Wang, S., & Wang, J. X. 2003, *MNRAS*, **345**, 809
 Makarov, V. I., & Sivaraman, K. R. 1986, *Kodaikanal Obs. Bull.*, **7**, 138
 McIntosh, S. W., Cramer, W. J., Pichardo Marcano, M., & Leamon, R. J. 2017, *NatAs*, **1**, 0086
 Mei, Y., Deng, H., & Wang, F. 2018, *Ap&SS*, **363**, 84
 Oloketuyi, J., Liu, Y., & Zhao, M. 2019, *ApJ*, **874**, 20
 Pap, J., Tobiska, W. K., & Bouwer, S. D. 1990, *SoPh*, **129**, 165
 Raphaldini, B., & Raupp, C. F. M. 2015, *ApJ*, **799**, 78
 Raphaldini, B., Seiji Teruya, A., Raupp, C. F. M., & Bustamante, M. D. 2019, *ApJ*, **887**, 1
 Rieger, E., Share, G. H., Forrest, D. J., Kanbach, G., Reppin, C., & Chupp, E. L. 1984, *Natur*, **312**, 623
 Riley, P., Baker, D., Liu, Y. D., Verronen, P., Singer, H., & Güdel, M. 2018, *SSRv*, **214**, 21
 Rossby, C.-G. 1939, *JMR*, **2**, 38
 Teruya, A. S. W., Raphaldini, B., & Raupp, C. F. M. 2022, *FrASS*, **9**, 856912
 Torrence, C., & Compo, G. P. 1998, *BAMS*, **79**, 61
 Xiang, N. B., Zhao, X. H., & Li, F. Y. 2021, *PASA*, **38**, e032
 Zaqarashvili, T. 2018, *ApJ*, **856**, 32
 Zaqarashvili, T. V., Albekioni, M., Ballester, J. L., et al. 2021, *SSRv*, **217**, 15
 Zaqarashvili, T. V., & Gurgenchvili, E. 2018, *FrASS*, **5**, 7
 Zaqarashvili, T. V., Oliver, R., & Ballester, J. L. 2009, *ApJL*, **691**, L41
 Zaqarashvili, T. V., Oliver, R., Ballester, J. L., et al. 2011, *A&A*, **532**, A139
 Zaqarashvili, T. V., Oliver, R., Ballester, J. L., & Shergelashvili, B. M. 2007, *A&A*, **470**, 815
 Zaqarashvili, T. V., Oliver, R., Hanslmeier, A., et al. 2015, *ApJL*, **805**, L14